Exploring the interactions of M dwarf winds and cosmic rays

Mesquita, A.L.

1
Introduction

In this thesis, I will discuss the interaction between M dwarf stellar winds and Galactic cosmic rays and the possible effects on the habitability of exoplanets. In particular, I have used numerical simulations to describe the stellar winds of M dwarfs using observable constraints, such as the mass-loss rate, X-ray luminosity, and magnetic field strength/flux. Additionally, I have also used numerical simulations to describe the propagation of Galactic cosmic rays within M dwarfs planetary systems. With these simulations, I was able to calculate the flux of Galactic cosmic rays reaching exoplanet magnetospheres/atmospheres. Measuring cosmic ray fluxes in exoplanet atmospheres is yet not possible, but cosmic rays are an important ingredient in the context of planetary habitability. For this reason, quantifying these fluxes is essential to complete the habitability "puzzle". Future exoplanet atmosphere observations with space telescopes, such as the James Webb Space Telescope (JWST) and the Atmospheric Remote-sensing Infrared Exoplanet Large-survey (ARIEL), will enable us to constrain cosmic ray fluxes in exoplanet atmospheres.

1.1 Habitable zone and exoplanet habitability

In the last few decades, more than 5000 exoplanets have been discovered. With so many exoplanets having been observed so far, there is a lot of interest in determining if any of these exoplanets are habitable. However, many factors are associated with the habitability of an exoplanet, such as planetary and stellar properties, stellar effects (see e.g., Meadows & Barnes, 2018) and determining if an exoplanet is habitable (or not) seems a complex problem. Fig. 1.1 shows a summary of the planet, stellar and planetary system properties that are believed to affect planetary habitability. The font colour indicates the way these properties can be obtained. Blue represents the properties that could possibly be observed, orange are properties that can be modelled using observable constraints and green are properties that can be theoretically modelled.

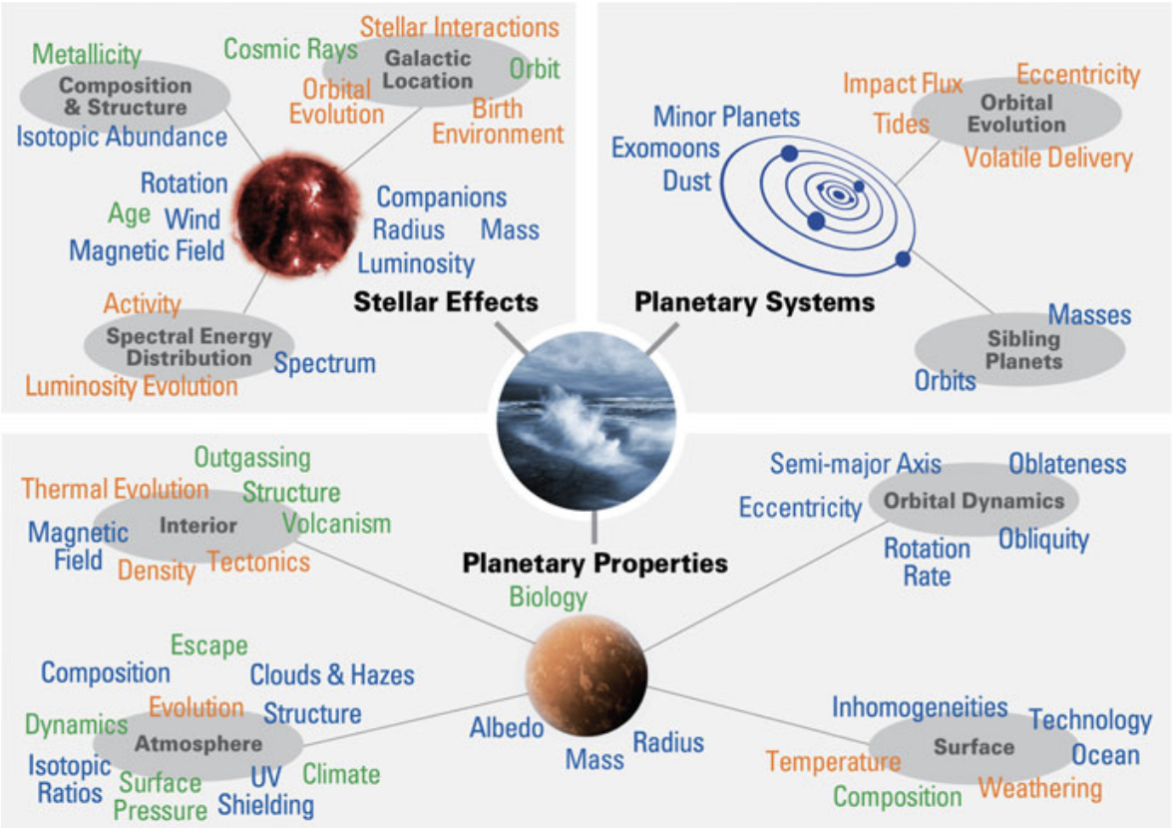

Figure 1.1: Diagram showing the possible factors affecting planetary habitability. In blue are shown possible observable properties while green are properties that require modelling with observational constraints. In orange are the properties which require theoretical modelling. Figure from Meadows & Barnes (2018).

One extremely important factor for life as we know it is the presence of liquid water[1] on the exoplanet's surface that can be influenced by many factors including properties of the stellar system and planet itself. The circumstellar region around a star in which a planet can sustain liquid water on its surface is commonly called the habitable zone (Kasting et al., 1993; Selsis et al., 2007). This region is close-in for small stars, such as M dwarfs, and further out for F and G dwarfs, such as our Sun. Being in the habitable zone is believed to be the first condition to be important for exoplanet habitability, although it does not necessarily mean that a planet in the habitable zone is habitable.

Fig. 1.2 shows the habitable zone as a function of the stellar mass for stars of solar metallicity and effective temperature between 3700 K and 7200 K. The dark grey region is the habitable zone defined by the empirical "early Mars" and "recent Venus" criteria

[1]Life as we know requires at least three ingredients: energy, "biogenic" elements (C, H, O, N and S) and a liquid solvent (see e.g., Hoehler et al., 2018). All Earth-based life needs liquid water as a solvent.

(cloud-free limits). The "recent Venus" criterion gives an empirical indication of the inner edge of the habitable zone. This criterion is due to the fact that surface maps of Venus indicate that liquid water has not been present on the planet in the last $\sim 1\,\mathrm{Gyr}$ (Solomon & Head, 1991). At that time, the luminosity of the Sun was believed to be around 8% dimmer than its present value[1]. Thus, the luminosity received by Venus, at that time, was equal to the one received today at a distance $\sim 0.75\,\mathrm{au}$ (Selsis et al., 2007). Similar to the inner edge, the outer edge of the habitable zone can be defined by empirical indication of the early Mars conditions. The "early Mars" criterion is due to the fact that geological and geochemical characteristics show that, around $\sim 4\,\mathrm{Gyr}$ ago, Mars was warm enough to have surface liquid water (Pollack et al., 1987; Bibring et al., 2006). The Sun's luminosity was 28% dimmer at that time, thus the flux received at Mars was equal to what it is today at a distance of $\sim 1.77\,\mathrm{au}$ (Selsis et al., 2007).

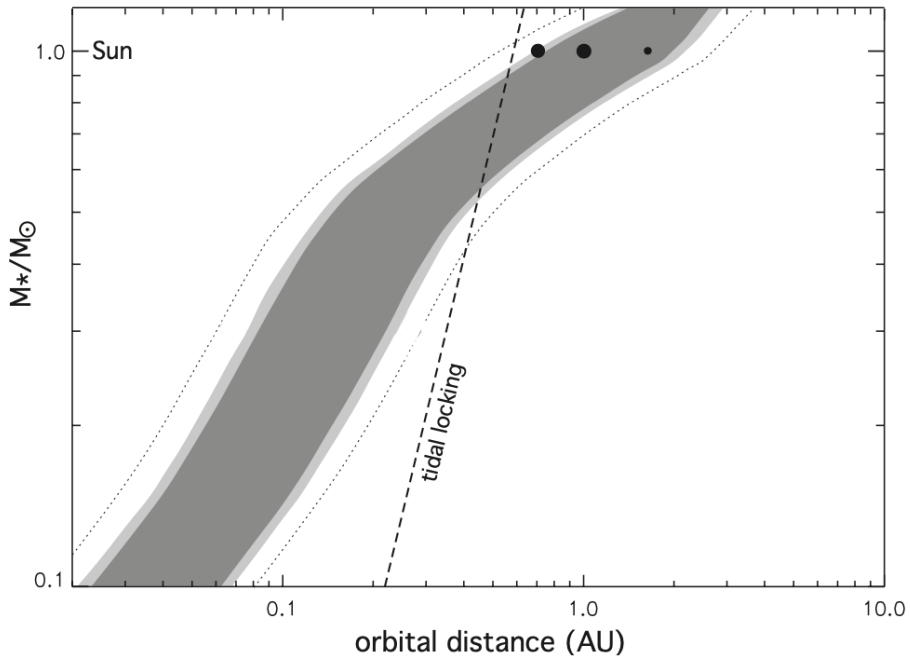

Figure 1.2: Habitable zone as a function of the stellar mass. The darker region represents the habitable zone defined by the empirical "early Mars" and "recent Venus" criteria. The light grey regions give the theoretical limits with 50% clouds and the dotted lines correspond to the theoretical limits with 100% cloud cover. The dashed line shows the distance ($\lesssim 0.7\,\mathrm{au}$) at which a $1\,M_\oplus$ planet becomes tidally locked in less than 1 Gyr. The black dots represent Venus, Earth and Mars, respectively. Figure modified from Selsis et al. (2007).

The light grey areas of Fig. 1.2 represent the theoretical limits with 50% cloud cover

[1]Solar evolution models have shown that during its lifetime in the main sequence, the Sun has slowly increased its luminosity (e.g., Neronov et al., 2017; Gough, 1981).

and the dotted lines give the theoretical limits with 100% cloud cover. H_2O-clouds can increase the planetary albedo and thus move the inner habitable zone boundary limits closer to the star by reducing greenhouse warming (Selsis et al., 2007). The presence of CO_2-clouds, on the other hand, can extend the outer habitable zone boundary limits by warming the planet's surface caused by a scattering variation of the greenhouse effect (Mischna et al., 2000; Selsis et al., 2007). The dashed line represents the distance ($\lesssim 0.7\,\mathrm{au}$) at which a $1\,M_\oplus$ planet becomes tidally locked (one side of the planet always faces the star, similar to the moon with respect to the Earth) in $< 1\,\mathrm{Gyr}$. This is particularly important for M dwarfs since planets within the habitable zone are expected to be tidally locked (Kasting et al., 1993). A tidally locked exoplanet can have a low heat distribution from the day side to the night that could affect the exoplanet's climate.

In the context of this thesis, any planet in the habitable zone will be called a potentially habitable planet. This is not the same as a "real" habitable planet, i.e., any other criteria except for the habitable zone will not be considered here.

1.2 M dwarfs

M dwarfs are by far the most common type of stars in our Galaxy, accounting for at least 70% of all the stars in our solar neighbourhood (Henry et al., 2006; Winters et al., 2015; Henry et al., 2018). They are small, main-sequence stars with masses in the range of $0.08 - 0.5\,M_\odot$, low effective temperatures ($< 4000\,\mathrm{K}$) and low brightness. All of these characteristics make M dwarfs the perfect candidates for observing exoplanets with current observing techniques, in particular rocky potentially habitable planets. Due to their low luminosities, M dwarfs present a good contrast to detect smaller-size exoplanets using the transit method, and their low masses enable the detection of lower-mass exoplanets using the radial velocity method. These exoplanet detection methods usually favour the detection of close orbiting planets.

M dwarfs are also interesting because of their close-in habitable zone which makes it easier to observe planets in these regions. The majority of planets observed around M dwarfs are located within 1 au. For these reasons, M dwarfs are currently the main targets in search of potentially habitable exoplanets. Our closest star, Proxima Centauri (Prox Cen), for instance, hosts an Earth-like planet in its habitable zone (Anglada-Escudé et al., 2016). Trappist-1 is another extremely interesting M dwarf system, as it hosts 7 planets with 4 of these planets orbiting within the habitable zone (Gillon et al., 2017).

One potential issue for exoplanet habitability is that a large fraction of main-sequence M dwarfs remain magnetically active for a longer fraction of their lives compared to solar-mass stars (West et al., 2004; Scalo et al., 2007; West et al., 2015; Guinan et al., 2016). The fraction of active M dwarfs is larger for later spectral types (e.g., West et al., 2008). Additionally, M dwarfs can generate strong kilogauss magnetic fields (Morin et al., 2010; Shulyak et al., 2019). Magnetic fields play an important role in interior (e.g., Mullan & MacDonald, 2001; Browning, 2008) and atmospheric properties (e.g., Kochukhov, 2021) of M dwarfs as well as influencing close-in exoplanets. Strong stellar magnetic activity can affect the stellar wind properties (Vidotto et al., 2014a), generate strong flares (Vida et al., 2017; Tilley et al., 2019), coronal mass ejections (Lammer et al., 2007; Khodachenko et al., 2007) and accelerate more high energy particles (Grießmeier et al., 2005). All of these phenomena can affect the exoplanets orbiting M dwarfs close-in habitable zones as well as planet habitability (Khodachenko et al., 2007; Vida et al., 2017; Tilley et al., 2019). Strong stellar winds can erode exoplanet atmospheres (e.g., Zendejas et al., 2010; Vidotto et al., 2013) while the longer exposure to stellar radiation and high energy particles can affect the planet's climate (e.g., Grenfell et al., 2013) and possibly the planetary atmosphere (e.g., Rimmer & Helling, 2013; Rimmer et al., 2014; Tabataba-Vakili et al., 2016; Scheucher et al., 2018).

1.2.1 Magnetic fields and stellar activity

Similar to the Sun, the magnetic fields of cool dwarfs are believed to be produced by the dynamo mechanism in the interface layer, known as tachocline, between the radiative zone and the convection zone (Charbonneau, 2014). The dynamo theory describes how the magnetic field is generated inside a star. The dynamo process is complex and not fully understood even for the Sun.

Not all M dwarfs have the tachocline layer in their interior. Two scenarios exist for the interior structure of M dwarfs and those are represented in Fig. 1.3. M dwarfs with $M \gtrsim 0.35\,M_{\odot}$ (early than M3.5 spectral type) have an interior similar to that of a solar-like star, with a radiative zone followed by a convective envelope. While M dwarfs with $M \lesssim 0.35\,M_{\odot}$ (later than M3.5 spectral type) have a fully convective interior (Chabrier & Baraffe, 1997). Despite not having a tachocline, low-mass fully convective stars also show magnetic activity and strong magnetic fields (Route, 2016; Reiners et al., 2022). Large-scale magnetic fields are starting to be observationally reconstructed for fully

convective stars (Morin et al., 2010; Morin, 2012; Klein et al., 2021a), even though it is still not fully understood how the magnetic fields are produced in these types of stars.

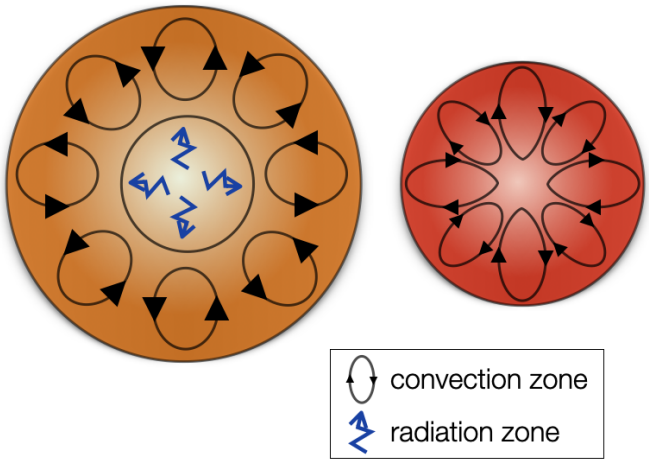

Figure 1.3: Schematic of stellar interior structure of M dwarfs. *Left*: partially convective interior, with radiative zone followed by a convective envelope. *Right*: fully convective interior.

For cool dwarfs, the large-scale magnetic field is believed to be generated by the $\alpha\Omega$ dynamo mechanism (Charbonneau, 2014). The convective zone is formed by plasma (a fluid of electrically charged particles) in continuous motion. The combination of electrically charged particles and motion creates electric currents, which generate magnetic fields, which in turn produce electric currents, and therefore a loop is generated. First, starting with a poloidal magnetic field, with a perpendicular direction, the stellar differential rotation stretches the magnetic field and winds it around the star, building a toroidal magnetic field with a horizontal direction (Ω-effect). Once the toroidal field has grown unstable, possibly due to cyclonic motions inside the star, the interaction of convection and rotation then restores a poloidal field with opposite polarity (α-effect).

In the solar case, the dynamo mechanism results in a magnetic activity cycle called the solar cycle (e.g., Hathaway, 2010). One of the best manifestations of the solar cycle is the sunspots[1] cycle. The solar cycle has a period of $\sim$ 11 years, which is characterised by an increase and decrease in the sunspot number. This period is also characterised by a flip in the north-south orientation of the solar large-scale magnetic field. Solar activity is distinguished by two periods: a solar minimum with weak magnetic activity and few or no sunspots visible on the solar surface and a solar maximum with strong magnetic activity and an increase in the number of sunspots visible.

[1]Sunspots are dark regions observed in the solar photosphere.

Other stars also show magnetic activity and measurements of the stellar magnetic field are essential to understand the dynamo process and also the many phenomena occurring in the stellar atmosphere due to magnetic activity. Photospheric magnetic fields can be directly observed by studying the Zeeman effect in which a single spectral line splits into multiple observable components due to the presence of a magnetic field. The splitting of the lines depends on the magnetic field strength. These spectropolarimetric observations show that M dwarfs can produce strong large-scale magnetic fields (Donati et al., 2006, 2008; Morin et al., 2008a,b, 2010; Hébrard et al., 2016; Moutou et al., 2017). Techniques such as Zeeman broadening and Zeeman Doppler Imaging (ZDI) are commonly used to understand the surface magnetic field properties of cool stars (e.g., Morin, 2012; Kochukhov, 2021). The Zeeman broadening method gives information on the unsigned surface magnetic field intensity ("total" magnetic field, large-scale and small-scale) while the ZDI method provides information on the large-scale stellar magnetic field geometry.

At this point, more than 300 M dwarfs have Zeeman broadening measurements (Kochukhov, 2021; Reiners et al., 2022) and more than 30 M dwarfs have ZDI observations (Donati et al., 2006, 2008; Morin et al., 2008a,b, 2010; Hébrard et al., 2016; Moutou et al., 2017). Fig. 1.4 shows the ZDI reconstruction of the large-scale magnetic field of Prox Cen with an average large-scale magnetic field of $\sim 200\,\mathrm{G}$ (Klein et al., 2021a). The average large-scale magnetic field of Prox Cen is 3 times smaller than the average Zeeman broadening measurements (Reiners & Basri, 2008). The magnetic field above the stellar surface can be calculated using the ZDI map as a boundary and a field extrapolation technique. Fig. 1.5 shows an example of the extrapolated magnetic field topology of Prox Cen using its ZDI map as the boundary for the surface large-scale magnetic field. Prox Cen shows a large-scale magnetic field geometry with dipole and quadruple components (Klein et al., 2021a).

X-ray emission is one of the traditional magnetic activity indicators which has been observed for many stars. Fig. 1.6 shows the correlation between X-ray luminosity and magnetic flux. The left panel shows the correlation from Zeeman broadening measurements (Pevtsov et al., 2003) and the right panel from ZDI measurements (Vidotto et al., 2014b). The magnetic field strength is proportional to magnetic flux, as $\Phi = 4\pi R_\star^2 B$, where $R_\star$ is the stellar radius. In both panels, the magnetic flux increases with X-ray luminosity which indicates that the large-scale field and the total field increase with X-ray luminosity. This relation suggests that coronal activities are powered by magnetic fields.

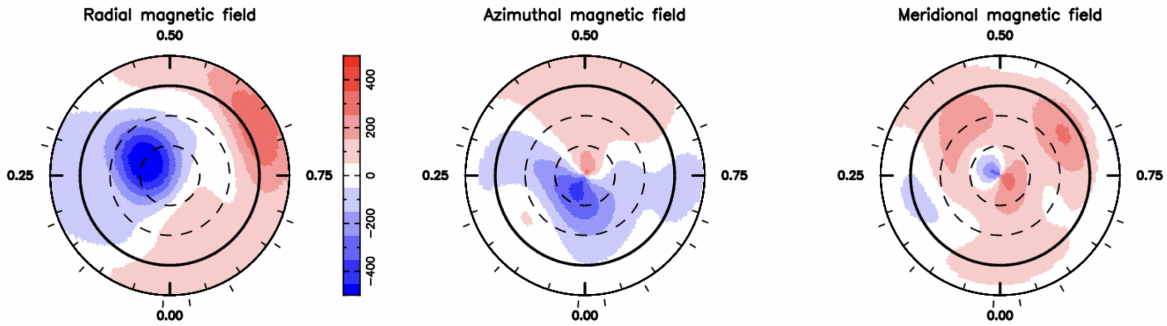

Figure 1.4: Surface distribution of the large-scale magnetic field topology of Prox Cen reconstructed with ZDI. From left to right the panels show the radial, azimuthal and meridional magnetic field components. Figure from Klein et al. (2021a).

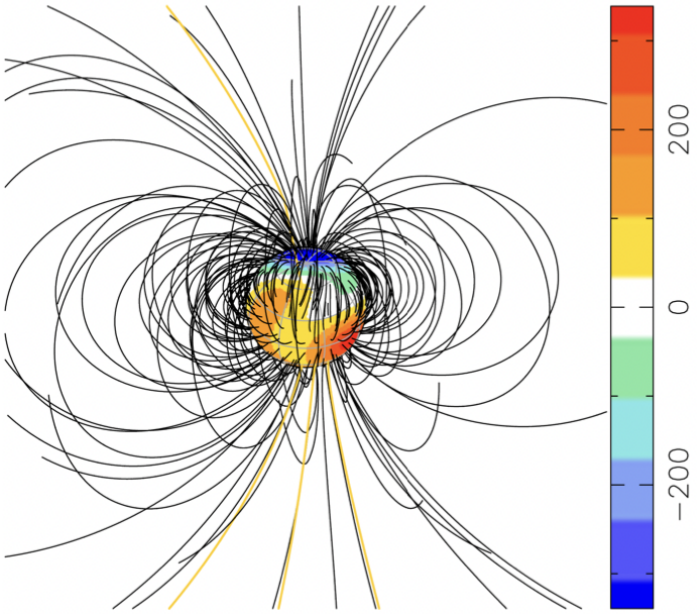

Figure 1.5: Large-scale magnetic field extrapolation of Prox Cen indicating the open and closed magnetic field lines. The color scale indicates the intensity of the radial magnetic field in Gauss. Figure from Klein et al. (2021a).

1.2.2 Stellar winds of cool dwarfs

Nearly all stars lose mass during their lifetimes in a process known as stellar wind. Stellar winds are the continuous outflow of material from the star surface (Lamers & Cassinelli, 1999). The stellar wind, and the stellar atmosphere dynamics, are dominated by the stellar magnetic field. Stellar winds play a key role in stellar evolution from the star's origin to its death (Matt et al., 2015; Johnstone et al., 2015). Stellar winds also interact with exoplanets.

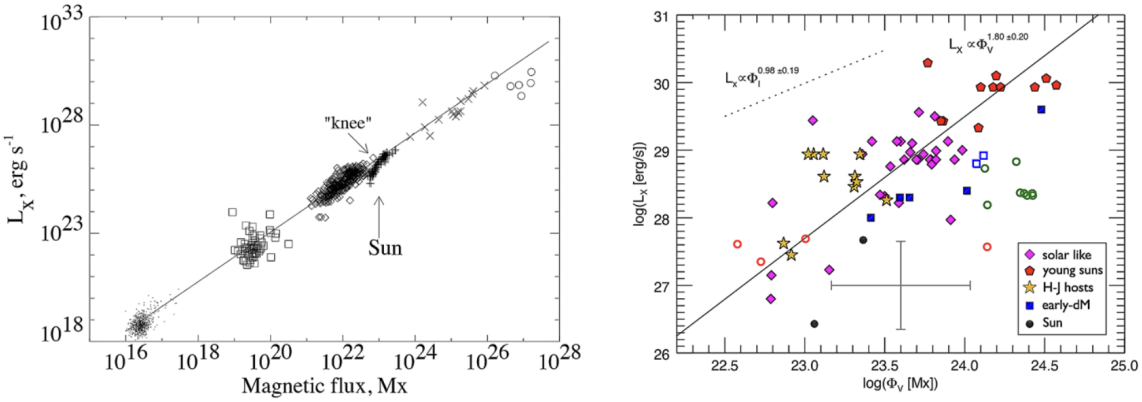

Figure 1.6: Correlation between X-ray luminosity and magnetic flux obtained from *Left*: Zeeman broadening measurements from Pevtsov et al. (2003). Dots represent the quiet Sun, squares the X-ray bright points, diamonds the solar active regions, crosses G, K, and M dwarfs, and circles the T Tauri stars. *Right*: ZDI measurements from Vidotto et al. (2014b). Open circles are the late and mid M dwarfs and are not considered in the fit. The solid lines in both panels are power-low fits.

1.2.2.1 Techniques to indirectly detect stellar winds

M dwarfs, similar to other cool dwarf stars, have very tenuous winds and, consequently, it is difficult to directly quantify them (Wood, 2004; Vidotto & Bourrier, 2017; Jardine & Collier Cameron, 2019). Fortunately, there are some techniques developed to indirectly infer the mass-loss rates of cool dwarfs. Here, I will briefly discuss some of the most successful techniques to infer mass-loss rates for cool dwarfs. A more in-depth review of the different methods can be found in Vidotto (2021).

The most successful method used to detect stellar winds is related to the study of stellar Ly-α absorption (Wood, 2004; Wood et al., 2021, and references therein). Ly-α absorption occurs when the stellar wind exchanges charges with a neutral (or partially neutral) interstellar medium (ISM). This absorption can be detectable in UV spectra. This technique favours stars within 7 pc from the Sun, because around this region the ISM is partially ionised making it possible to detect the astrospheric[1] Ly-α absorption. Beyond 7 pc the Local Bubble (which extends to ~ 100 au) is mainly fully ionised (Welsh et al., 2010).

Fig. 1.7 shows the example of α Cen B. The top panel shows the path of the stellar photons from the star towards the Sun. The middle panels show the Ly-α line profile as photons pass through the astrosphere, the ISM and the heliosphere. The purple

[1]Associated with the astrosphere which is analogous to the Sun's heliosphere. The concept of an astrosphere will be discussed in Section 1.3.

regions indicate the fraction of the line absorbed in each region. The bottom panel shows the observed Ly-α profile for α Cen B. The solid line is the assumed intrinsic stellar spectrum and the dashed line is the ISM profile. The shaded regions are the excess absorption due to the astrosphere (red region) and heliosphere (green region).

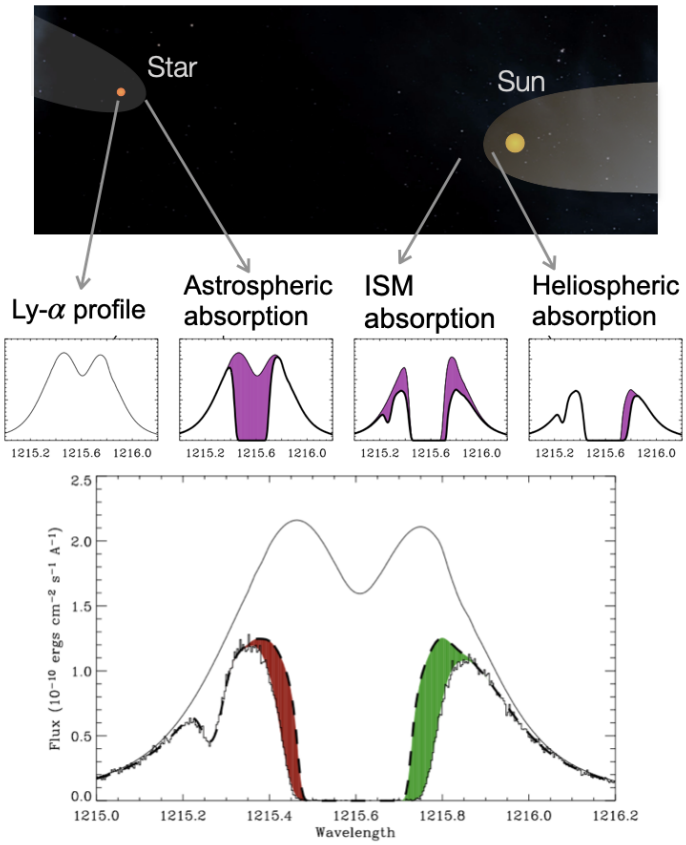

Figure 1.7: Schematic diagram of Lyman-α absorption observation. The top panel shows the Ly-α profile path from the star to the Sun. The middle panel shows how the Ly-α profile changes as it passes through the stellar astrosphere, the ISM and the heliosphere. The purple regions are the profile absorbed in each region. The bottom panel shows the observed Ly-α profile of α Cen B. The solid line is the assumed emission profile and the dashed line is the ISM line profile. The shaded regions show excess absorption from astrospheric absorption (red) and heliospheric absorption (green). Figure modified from Wood (2004).

By conducting and modelling Ly-α observations it is possible to estimate the wind ram pressure, $P_{\rm ram}$ (Wood et al., 2001). The mass-loss rate, $\dot{M}$, assuming spherical symmetry, can be determined by knowing the stellar wind terminal velocity, u_∞, from the relation

$$\dot{M} = \frac{4\pi R^2 P_{\rm ram}}{u_\infty}, \tag{1.1}$$

where R is a given reference distance where the wind has reached its terminal velocity. By assuming the Sun's asymptotic wind velocity of 400 km s^{-1} for all the stars in their sample, the method employed by Wood and collaborators Wood et al. (e.g., 2021) has estimated the mass-loss rate of nearly 30 stars. Almost half of this sample are M dwarfs. Some of the stars only have a mass-loss rate upper limit since the astrospheric absorption was not detected. That is the case, for instance, of Prox Cen with an inferred upper limit of $\dot{M}$. Prox Cen has a mass-loss rate ~ 0.2 times smaller than the solar wind mass-loss rate (Wood et al., 2001).

Another proposed method to infer the stellar mass-loss rate is the use of planet-wind interaction (Vidotto & Bourrier, 2017). This method favours planets with strong atmospheric escape, in particular close-in gas giant planets. The evaporating planet's atmosphere can be observed in Ly-α line absorption during its transit. By modelling the Ly-α line profile it is possible to obtain the local stellar wind properties. Three stars have had their mass-loss rates constrained using this technique but only one of these is an M dwarf (Bourrier & Lecavelier des Etangs, 2013; Kislyakova et al., 2014; Vidotto & Bourrier, 2017).

The study of slingshot prominences is another method used to derive mass-loss rates of cool dwarfs (Jardine & Collier Cameron, 2019). A slingshot prominence is a very extended, bright feature extending outward from the stellar surface. This technique is successful for very fast rotating stars (Villarreal D'Angelo et al., 2018). The slingshot prominences can be detected in H-α line absorption transients as the star rotates. These transients are associated with built up material trapped within large prominences above the stellar surface (Collier Cameron & Robinson, 1989). The mass trapped in the prominence and its lifetime can be determined with H-α observations. These two quantities are then used to infer the mass of the upflow in the prominence. The stellar mass-loss rate is then estimated by knowing the prominence surface coverage. Five stars have had their mass-loss estimated using this method with mass-loss rates 2-4 orders of magnitude higher than the solar values. These fast rotating stars are very active with larger X-ray fluxes and larger mass-loss rates than the Sun.

Other techniques, such as the study of thermal radio emission from stellar winds can provide measurements of stellar wind densities (Panagia & Felli, 1975). However, due to non-detections, this method has so far only been used to derive an upper limit for mass-loss rates (Lim & White, 1996; Gaidos et al., 2000; Fichtinger et al., 2017; Vidotto & Donati, 2017).

Fig. 1.8 show the mass-loss rates derived with different methods as a function of the stellar X-ray flux. The red circles are the quantities derived using Ly-α observations

for M dwarfs. The green circles are the same for G and K dwarfs and the blue squares for subgiants/giants stars (Wood et al., 2021). The red circle #16 was derived using the exoplanet-wind interaction (Vidotto & Bourrier, 2017). The magenta squares are derived from prominences (Jardine & Collier Cameron, 2019). The arrows represent upper limits for the mass-loss rate. The dashed line is the power-law fit to the data excluding the subgiants/giants stars (shown in black).

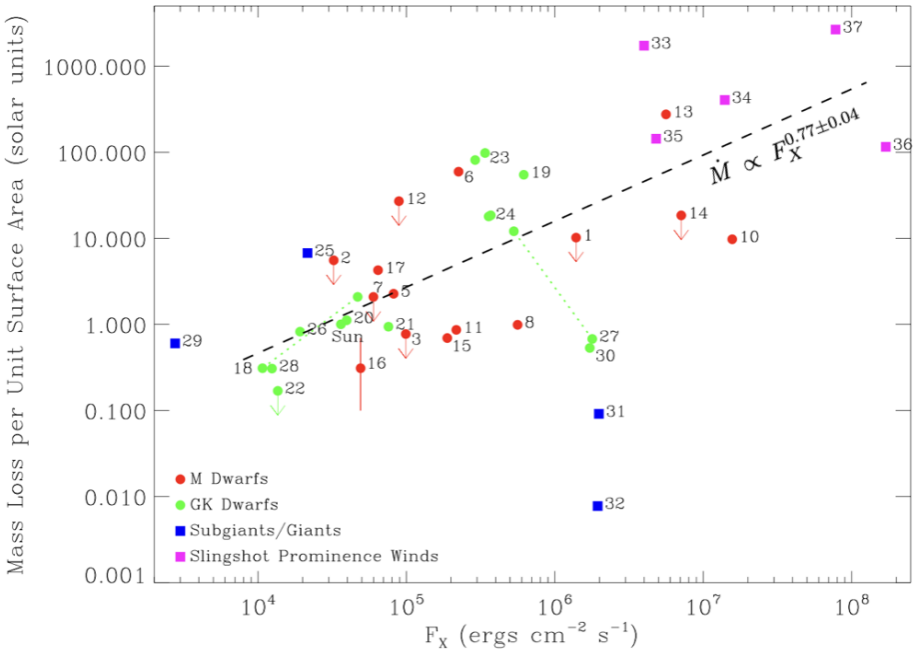

Figure 1.8: Mass-loss rates derived for low-mass stars as a function of X-ray flux. The circles and the blue squares are values derived with Ly-α observations. The red symbols are M dwarfs, the green G and K dwarfs and the blue are subgiants/giants stars. The magenta squares are values derived using prominences (Jardine & Collier Cameron, 2019). The red circle #16 was derived using the exoplanet as a probe of the stellar wind (Vidotto & Bourrier, 2017). The mass-loss rate is expressed in terms of solar wind units where $\dot{M}_\odot = 2 \times 10^{-14}\, M_\odot$ yr^{-1}. The dashed line is a power-law fit excluding the blue squares. Figure from Wood et al. (2021).

Mass-loss and coronal X-ray emission are both phenomena associated with the corona. $\dot{M}$ is associated with a wind that originates from open field lines (coronal holes). On the other hand, F_X originates from close field lines (bright regions in X-ray and UV images). Overall, mass-loss increases with X-ray luminosity, $\dot{M} \propto F_X^{0.77}$, but with some scatter as seen in Fig. 1.8. This may indicate that coronal activity and spectral type are not enough to explain stellar wind properties (Wood et al., 2021).

1.2.2.2 What drives the wind of M dwarfs?

X-rays are usually used as a magnetic proxy (see Section 1.2.1) and the relation shown by Wood et al. (2021) suggests a link between mass-loss rate and X-ray flux (see Section 1.2.2.1), which means that mass-loss is also magnetic in nature. However, there is still no agreement about which physical mechanisms of magnetic nature are responsible for heating and accelerate the winds of cool dwarfs, and even in the case of the solar wind it remains an open question (e.g., Cranmer, 2009; Cranmer & Winebarger, 2019). The study of the solar wind is important to better understand other stellar winds. Some mechanisms have been suggested to explain how stellar winds of cool dwarfs are driven.

From solar observations, it is known that the corona has a higher temperature than the solar surface (photosphere). This temperature gradient can be described by a thermally-driven wind, in which the physical reason behind the temperature increase from the photosphere to the corona is not taken into consideration. Instead, it assumes the corona has already reached around a million-Kelvin temperature before the wind is launched. A thermally driven wind usually uses a polytropic index to indicate the relation between temperature (or thermal pressure) and density to describe the temperature profile. In the case of an index equal to one, the wind is isothermal or a Parker wind (Parker, 1958). An isothermal wind description is commonly adopted to study winds of cool dwarfs due to its "simplicity". The only forces operating in the wind, in this case, are the gravity and the gradient of thermal pressure. A thermally-driven wind can include or not the effects of a magnetic field.

Another possibility is the use of MHD waves capable of naturally increasing the temperature from the photosphere to the corona and driving the outflowing stellar wind via the propagation of Alfvén waves. Magnetohydrodynamic (MHD) waves were first suggested as being associated with the presence of sunspots on the solar surface by Alfvén (1942). At this point, it was hypothesised that some type of MHD waves originating in the lower layers of the Sun was responsible for the photospheric activity observed. Only later were these MHD waves named after Hannes Alfvén. In 1949, Schatzman (1949) proposed that MHD waves could be the mechanism responsible for heating the solar corona to a higher temperature than the solar surface.

Alfvén waves propagate with an Alfvén velocity,

$$v_A = \frac{B}{\sqrt{4\pi\rho}}, \tag{1.2}$$

where B is the stellar wind magnetic field and ρ is the stellar wind density. Alfvén waves are generated by oscillations induced in the magnetic field lines at the base of the stellar wind. Fig. 1.9 presents a sketch of a stellar atmosphere where the open magnetic field lines oscillate and generate Alfvén waves. The stellar corona can be heated and accelerated by the dissipation of energy and momentum associated with the propagation of Alfvén waves, generating a stellar wind outflow (Hartmann & MacGregor, 1980; Vidotto & Jatenco-Pereira, 2006).

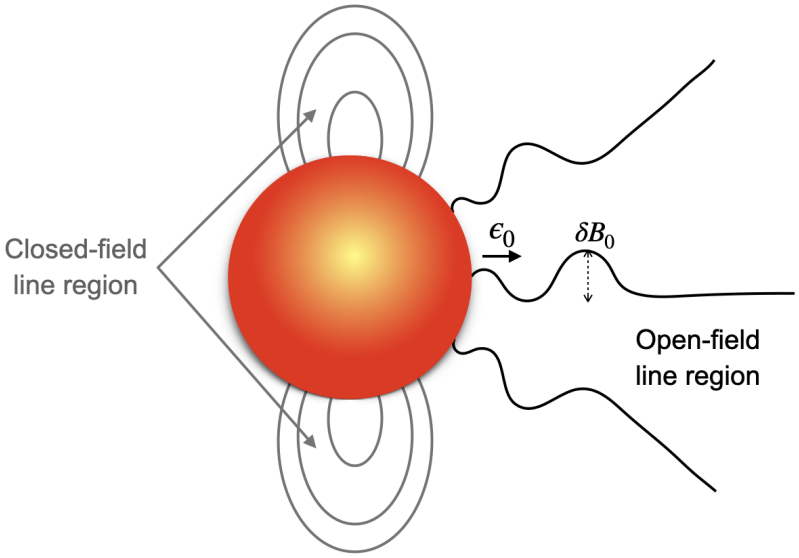

Figure 1.9: Schematic diagram of stellar atmosphere showing the closed and open magnetic field line regions. The open magnetic field lines oscillate in the form of Alfvén waves due to perturbations induced at the base of the wind. The amplitude of the wave depends on the magnetic field perturbation (δB_0) and the wave energy density at the base is given by ϵ_0.

Alfvén waves can be used to describe outflows in the form of an Alfvén-wave-driven wind. This approach includes the effects of magnetic fields. In this type of stellar wind models, it is possible to derive the detailed structure of the wind energetics, such as cooling and heating, contrary to a Parker wind, which assumes a wind temperature a priori. In this thesis, I assume that the winds of M dwarfs are heated and accelerated by magnetic processes. To implement this process, I use a stellar wind model that considers the presence of Alfvén waves to heat and accelerate the winds of M dwarfs.

It is known that Alfvén waves can transport energy to contribute to the coronal heating, but it is still unclear how the wave energy is converted into thermal energy and if the energy from the waves is enough to heat up the solar corona (Pagano & De

Moortel, 2019; Prokopyszyn et al., 2019). Tomczyk et al. (2007) reported the detection of Alfvén waves in the solar corona, but they estimated that the energy carried out by the waves was not enough to heat the corona. Although this might not be the only mechanism, Alfvén waves are still believed to be one of the main contributors to explain the temperature gradient in the Sun's atmosphere (e.g., Winebarger & Warren 2004; De Moortel & Browning 2015).

1.3 The interaction between the interstellar medium and the stellar wind

The solar wind interaction with the ISM creates a vast bubble-like shaped region around the Sun called the heliosphere. The region inside the heliosphere is dominated by the solar wind while the outside region is dominated by the interstellar wind. Similar to the solar wind, stellar wind interaction with the ISM also leads to the formation of an astrosphere. It is because of these interactions that stellar winds can be detected using Ly-α line observations (see Section 1.2.2.1).

Fig. 1.10 shows a sketch of a bubble-like shaped astrosphere. When the stellar wind starts to interact with the ISM, its velocity slows down. The region where the stellar wind properties start to change due to the interaction with the ISM is called the termination shock. The boundary where the ISM and stellar wind pressures are balanced is called the astropause. The pressure balance can be calculated as,

$$\begin{aligned} P_{\rm ram} &= P_{\rm ISM} \\ \frac{\dot{M} u_\infty}{4\pi R^2} &= m_p n_{\rm ISM} \nu_{\rm ISM}^2, \end{aligned} \tag{1.3}$$

where m_p is the proton mass, $n_{\rm ISM}$ is the total ISM number density of hydrogen and $\nu_{\rm ISM}$ is the ISM velocity as observed by the star. $P_{\rm ram}$ can be expressed in terms of Equation (1.1) because at large distances, where the wind has reached its terminal velocity, the density of the wind falls with r^{-2} and $P_{\rm ram}$ follows the same trend.

Equation (1.3) allows us to calculate the extension of the astrosphere, $R_{\rm ast}$, in terms of the stellar mass-loss rate, as

$$R_{\rm ast} = \left(\frac{\dot{M} u_\infty}{4\pi m_p n_{\rm ISM} \nu_{\rm ISM}^2} \right)^{1/2}. \tag{1.4}$$

Thus, the astrospheric size is not only influenced by the stellar wind properties but also by the ISM properties, such as density, velocity and ionisation fraction. In addition,

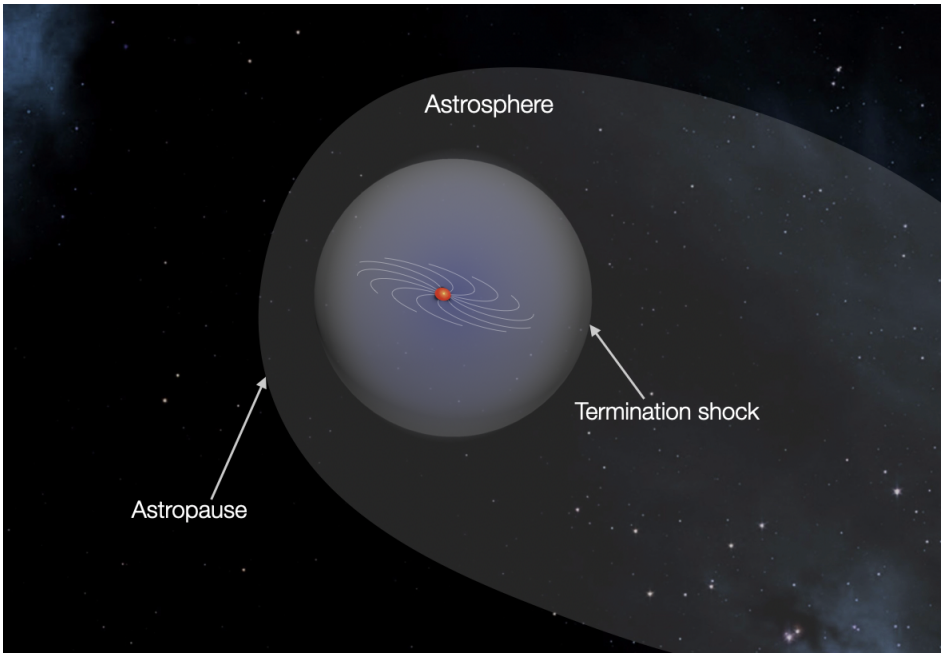

Figure 1.10: Schematic of an astrosphere shaped by the interaction between the ISM and the stellar wind. The termination shock is the region where the stellar wind properties start to change due to the interaction with the local ISM and the astropause.

the astrosphere can change in response to the Galactic environment around the star since the star moves through the ISM.

The heliosphere is located in the Local Interstellar Cloud (LIC) inside the Local Bubble. The LIC is the cloud immediately surrounding the Sun roughly 5-7 pc across (Redfield & Linsky, 2000) while the Local Bubble is the low density region within ~ 100 pc of the Sun. Fig. 1.11 shows the solar system within the LIC along with other stellar systems (blue dots) and stars with detected astrospheres (yellow bubble-like shape symbols).

Since the ISM can have different properties in different locations of the Galaxy, this change can directly impact the astrosphere size. Some works have investigated the astrosphere response under different ISM scenarios for both general astrospheres (Jasinski et al., 2020) and the heliosphere (Scherer et al., 2002, 2008; Müller et al., 2006). Müller et al. (2006) found that the extent (or size) of the heliosphere and structure can be vastly influenced by different ISM properties while assuming the same properties for the solar wind. In their model, the heliopause location was found to vary from 12 au, for an ISM $\sim 3\times$ denser and $\sim 4\times$ faster than contemporaneous values, to 402 au, for an ISM $\sim 3\times$ slower than contemporaneous values. Currently, the heliosphere extends to ~ 122 au as observed by *Voyager 1* (Stone et al., 2013, 2019).

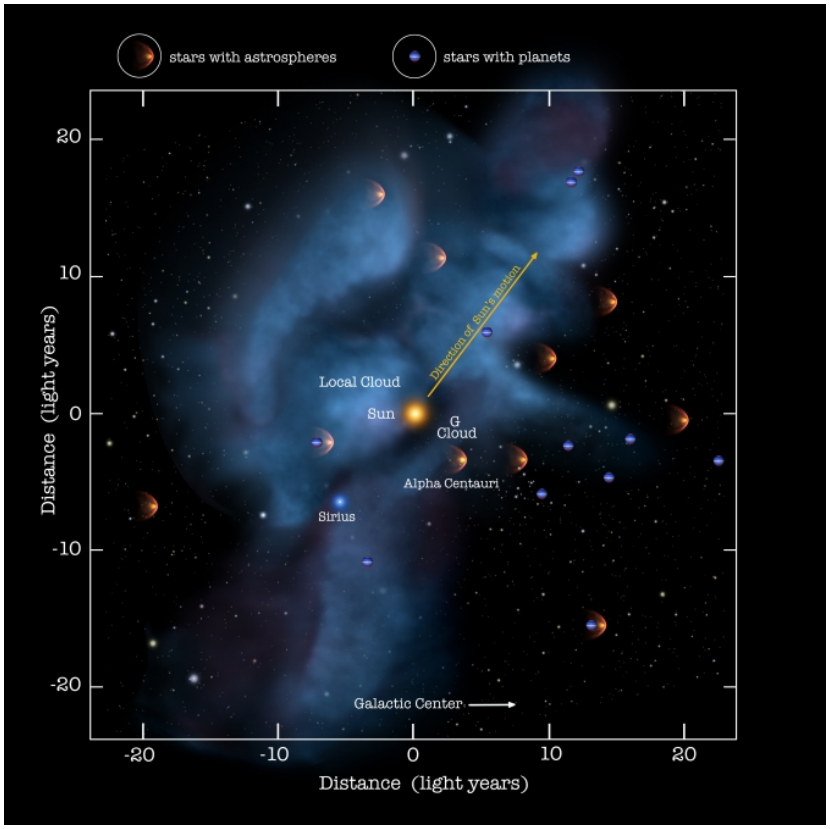

Figure 1.11: Local Interstellar Cloud structure. The solar system is shown in the center and its motion direction is shown by the yellow arrow. The yellow bubble-like shape symbols represent other detected astrospheres and the blue dots represent stars with known exoplanets. The direction of the Galactic Center is indicated by the white arrow. Image Credits: NASA/Adler/U. Chicago/Wesleyan.

On the other hand, Rodgers-Lee et al. (2020) investigated the heliosphere response due to changes in the solar wind for different ages of the solar system (while assuming the same properties for the ISM). They found that the heliopause distance decreased as the Sun aged varying from ~ 1530 to 47 au.

In terms of stars, astrosphere sizes can vary from a few au to 10^3 au (Herbst et al., 2020; Rodgers-Lee et al., 2021b; Mesquita et al., 2021, 2022a,b). Similar to the heliosphere, the astrosphere size can change as the star passes through different ISM regions and also when the star gets old and starts to be less active. All of these changes are especially important in the context of Galactic cosmic ray propagation inside stellar systems (see Section 1.4).

1.4 Galactic cosmic rays and stellar wind interaction

Cosmic rays are high-energy particles originating from the Sun (stellar cosmic rays), in our own Galaxy (Galactic cosmic rays), and outside our Galaxy (extra-galactic cosmic rays, Blasi, 2014). Galactic cosmic rays fill and are constantly present in the entire Galaxy. They mainly originate from, or are accelerated by, supernova remnant shocks formed in the ISM as the result of supernova explosions (Enomoto et al., 2002; Aharonian et al., 2004; Brose et al., 2020). It is assumed that cosmic rays with energy up to $\sim 10^{15}$ eV are from our own Galaxy, while the extra-galactic cosmic rays have much higher energy ($\sim 10^{18}$ eV) (Blasi, 2014). The origin of such high-energy cosmic rays is still unknown (Alves Batista et al., 2019). Stellar cosmic rays, also known as stellar energetic particles, originate in stellar events such as flares and coronal mass ejections (Rodgers-Lee et al., 2021b). Stellar cosmic ray typical energies can vary accordingly with stellar activity. For instance, during strong solar flares, the present-day Sun, an inactive star, can accelerate particles to $\sim 10^{9}$ eV energies (Ajello et al., 2014; Kafexhiu et al., 2018).

In this work, I will only focus on Galactic cosmic ray protons. Galactic cosmic rays can penetrate the astrosphere and reach planet magnetosphere/atmospheres. When interacting with planet atmospheres, cosmic rays can produce showers of secondary particles, which can reach the planet's surface. Fortunately, the magnetised stellar wind throughout the astrosphere acts as a barrier to Galactic cosmic ray fluxes. Outside the astrosphere, the Galactic cosmic ray has its background level (see Section 1.4.2), while inside the astrosphere it is modulated in an energy-dependent way. The modulation of cosmic rays can be explained as follows: to penetrate inside the astrosphere, Galactic cosmic rays need to overcome the outward flow of magnetised and turbulent stellar wind plasma. The magnetised stellar wind prevents low-energy cosmic rays from freely propagating into the inner astrosphere while high-energy cosmic rays are nearly unaffected (Parker, 1965; Potgieter, 2013).

When interacting with exoplanet atmospheres, cosmic rays can ionise molecules and lead to the production of prebiotic molecules (Dartnell, 2011; Rimmer et al., 2014; Airapetian et al., 2016; Barth et al., 2021). These prebiotic molecules are associated with the start of life. Thus, cosmic rays may have been associated with the emergence of life at Earth and possibly in other exoplanets (Airapetian et al., 2016; Atri, 2016). Many works have suggested cosmic rays can also affect Earth's climate through cloud coverage (Svensmark & Friis-Christensen, 1997; Shaviv, 2002, 2003; Kirkby et al., 2011; Svensmark et al., 2017).

Additionally, cosmic rays can also affect developed life-forms by causing cellular mutation (Dartnell, 2011) and damaging DNA in cells (Sridharan et al., 2016). The influence of cosmic rays on life-forms can be quantified by the planetary radiation dose (Atri, 2020; Atri et al., 2020). The planet's surface is protected by the presence of an atmosphere and possibly a magnetosphere and the majority of cosmic rays do not reach the surface. It has been shown that magnetospheres (Grenfell et al., 2007; Grießmeier et al., 2009, 2015) and atmospheres (Grießmeier et al., 2016; Atri, 2020) can lessen cosmic ray fluxes at the planetary surface. In contrast, the lack of a planetary magnetic field can enhance cosmic ray intensities by more than three orders of magnitude (Grießmeier et al., 2015). The radiation dose on the planet's surface can also be affected by the depth of the planet's atmospheric column density (Atri et al., 2013; Atri, 2017). A larger atmospheric depth is effective at reducing the radiation dose at the planet's surface (Atri, 2020). The radiation dose is therefore distributed further up in the atmosphere.

1.4.1 Galactic cosmic ray observations at Earth and correlation with solar activity

Cosmic rays fluxes are an important element in exoplanet habitability and quantifying their fluxes is essential (as described in Section 1.4). Galactic cosmic ray fluxes reaching Earth have been measured by different instruments at different times as shown in Fig. 1.12. The dotted line is representative of the unmodulated Galactic cosmic ray spectrum outside the heliosphere (see Section 1.4.2). The symbols indicate measurements made by different instruments. Red, yellow and blue symbols and shaded regions indicate approximately maximum, moderate and minimum solar activity regimes. The observations span over 40 years, and the differential intensity of cosmic rays varies by two orders of magnitude over the solar cycle. The cosmic ray intensity exhibits a link with the solar activity in which during solar minimum more cosmic rays are detected and during solar maximum cosmic rays are strongly suppressed.

The anti-correlation between the solar 11-year activity cycle and the intensity of Galactic cosmic rays at Earth is shown in Fig. 1.13. The top panel shows the percentage of cosmic rays observed at Earth in different epochs for particles with a cut-off momentum of 4.6 GeV/c. The values are normalised to 100% in March 1987. The bottom panel shows the yearly average sunspot number observed for five solar minimum activity periods (indicated by vertical lines). The heliospheric magnetic field polarity (A) epoch is also indicated at the top of Fig. 1.13. $A > 0$ indicates epochs in which

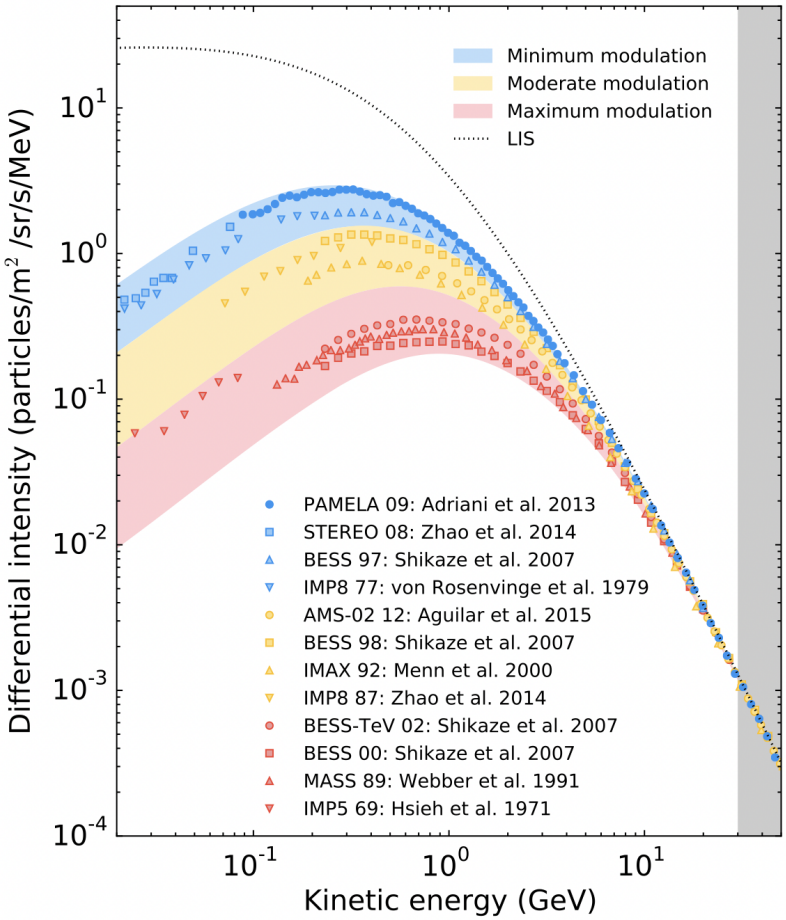

Figure 1.12: Galactic cosmic ray fluxes reaching Earth observed by different instruments throughout many years. Blue, yellow and red points are associated with minimum, moderate and maximum solar activity, respectively, which is anti-correlated with Galactic cosmic ray intensity. The dotted line is representative of the unmodulated Galactic cosmic ray spectrum. The grey shaded region indicates where suppression can be considered negligible. Figure from Vos & Potgieter (2015).

the solar magnetic field is pointed outward in the northern and inward in the southern polar region. Fig. 1.14 shows a schematic of these magnetic field polarity epoch configurations.

From Fig. 1.13 it is possible to observe that the magnetic field polarity epoch seems to affect the cosmic ray count. During solar minimum periods with $A < 0$ (solid and dashed lines), the cosmic ray count shows a sharp maximum while for periods with $A > 0$ (dotted and dash-dotted lines) an almost plateau is observed. This behaviour is attributed to particle drift effects (e.g, Strauss et al., 2012; Potgieter, 2013; Potgieter & Vos, 2017), a topic that will be discussed in Chapter 5.

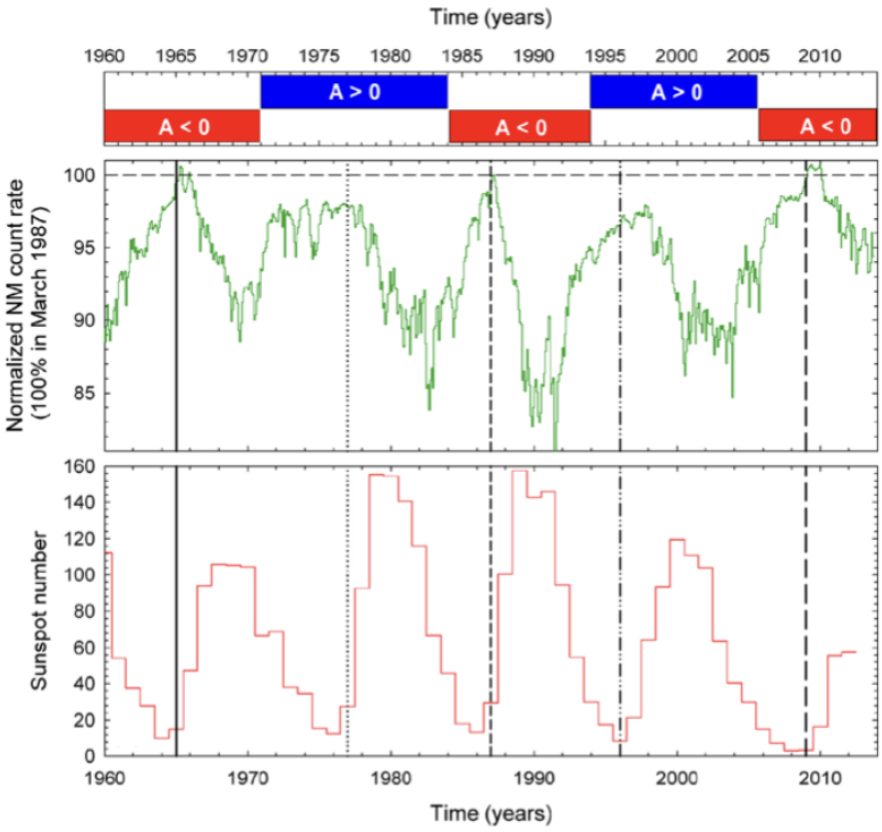

Figure 1.13: The top panel shows the solar modulation of cosmic rays observed by the Hermanus cosmic ray monitor in South Africa for a period of $\sim$ 50 year, with counts normalised to 100% in March 1987. The bottom panel shows the yearly averaged sunspot number for the same period. The vertical lines indicate approximate times of solar minimum. The magnetic field polarity (A) is also indicated at the top. Figure from Strauss & Potgieter (2014).

1.4.2 The Local interstellar spectrum

Outside of the astrosphere, Galactic cosmic rays are not suppressed by the stellar outflow and have their background level. This background level is important because it sets the maximum flux of Galactic cosmic rays at the astropause boundary (assuming the star is not near a cosmic ray source). In August 2012, *Voyager 1* crossed the heliopause[1] and measured the cosmic ray intensity in the local ISM (Stone et al., 2013). These measurements are believed to be largely unaffected by the solar wind (Stone et al., 2013; Cummings et al., 2016) and represent the local interstellar spectrum (LIS) for cosmic rays with energy between 3 and 600 MeV. Vos & Potgieter (2015) developed

[1]In 2012, *Voyager 1* crossed a region where it experienced a sharp drop in energetic heliospheric ions and an increase in low-energy Galactic cosmic rays protons, indicating it had crossed the heliopause (Stone et al., 2013).

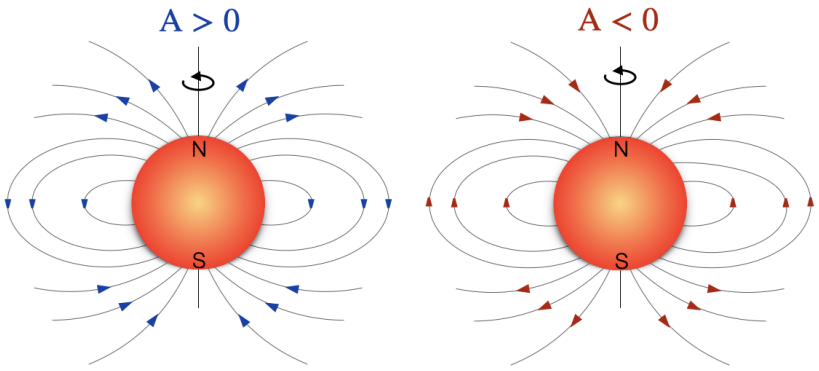

Figure 1.14: Schematic of the large-scale magnetic field polarity epochs. Magnetic field directed outward from the star in the northern polar region and inward in the southern polar region are known as A $>$ 0, while A $<$ 0 indicates the reverse magnetic field geometry.

a model fit, using the *Voyager 1* observations, to represent the cosmic ray differential intensities of the LIS, $j_{\rm LIS}$,

$$j_{\rm LIS}(T) = 2.70 \frac{T^{1.12}}{\beta^2} \left(\frac{T + 0.67}{1.67} \right)^{-3.93} \ {\rm m}^{-2}{\rm s}^{-1}{\rm sr}^{-1}{\rm MeV}^{-1}, \tag{1.5}$$

where T is the kinetic energy of the cosmic rays in GeV and $\beta = v/c$ is the particle speed as a fraction of the speed of light. Equation (1.5) represents the amount of Galactic cosmic rays at the heliopause at 122 au. Fig. 1.15 shows the *Voyager 1* observations of the LIS (green and yellow diamonds) and observations of cosmic rays at Earth using PAMELA (red circles) and AMS-02 (blue circles). Galactic cosmic rays with energies above 30–50 GeV are virtually unsuppressed by the solar wind (e.g., Potgieter, 2013; Vos & Potgieter, 2015) and measurements at Earth can be used to further constrain the LIS at this energy range. The model fit to the LIS is shown in Fig. 1.15 by the black line.

Unfortunately, in-situ measurements of Galactic cosmic ray fluxes in locations other than the solar system are not available. However, Galactic cosmic rays, with GeV energy, can be indirectly detected by observing γ-ray emission. As cosmic rays travel in the Galaxy, they interact with matter, and this interaction generates γ-ray emission. Many works have used γ-ray observations of nearby molecular clouds to infer the cosmic ray intensities in other locations in the Galaxy (Neronov et al., 2017; Aharonian et al., 2020; Baghmanyan et al., 2020) and it was found that γ-ray observations, with energy $\sim 10 - 10^4$ GeV, across a region of 1 kpc in the local Galaxy are consistent with the LIS measurements (Neronov et al., 2017). Some local variations in the cosmic ray spectrum

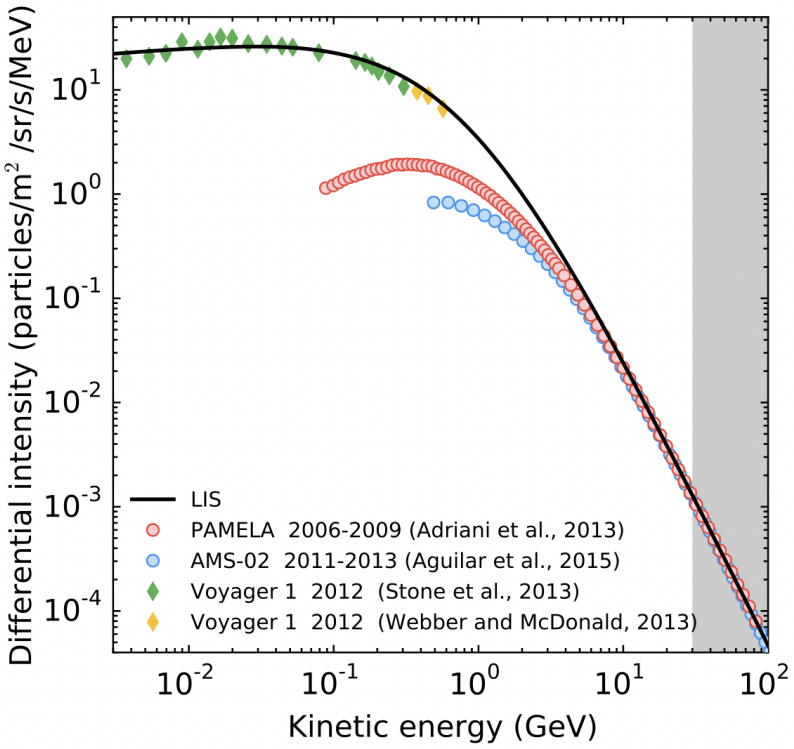

Figure 1.15: Differential intensity of Galactic cosmic rays as a function of kinetic energy. The diamond points are observations by *Voyager 1* while it is orbiting outside the heliosphere. The circles are observations at Earth made by PAMELA (red circles) and AMS-02 (blue circles). The black line is a model fit to the observations representative of the unmodulated cosmic ray outside the heliosphere, known as the LIS. Figure from Vos & Potgieter (2015).

are expected in the Galactic disk (Baghmanyan et al., 2020), mainly near acceleration regions, which can show a local increase in the cosmic ray flux (Fatuzzo et al., 2006). This allows us to use LIS observations outside the heliosphere to describe the Galactic cosmic ray spectrum outside other astrospheres if they are not near any cosmic ray accelerator region.

1.4.3 How to infer/detect cosmic rays on other planets

To understand the effect of cosmic rays on exoplanet habitability it is necessary to estimate their intensities at the planet's magnetosphere, atmosphere, and/or surface. Cosmic ray transport models are currently the only approach to quantify the intensity of Galactic cosmic rays reaching exoplanets (e.g., Sadovski et al., 2018; Herbst et al., 2020; Mesquita et al., 2021; Rodgers-Lee et al., 2021b; Mesquita et al., 2022a,b) and the Earth focusing on different ages of the solar system (e.g., Scherer et al., 2002, 2008;

Müller et al., 2006; Svensmark, 2006; Cohen et al., 2012; Rodgers-Lee et al., 2020). Many works have used cosmic ray models to understand the fluxes observed at Earth (e.g., Potgieter, 2013; Strauss et al., 2012; Strauss & Potgieter, 2014; Potgieter et al., 2015a). Similarly, models have also been used to understand the effects of stellar cosmic rays in exoplanet's atmospheres (Segura et al., 2010; Grenfell et al., 2012; Tabataba-Vakili et al., 2016; Scheucher et al., 2020) and in M dwarf habitable zone (Fraschetti et al., 2019).

Cosmic rays are a source of ionisation in exoplanet atmospheres and some fingerprint ions, such as H_3O^+, H_3^+ and NH_4^+ (Helling & Rimmer, 2019; Barth et al., 2021) have been identified as good indicators of the presence of cosmic rays (both Galactic and stellar counterparts) in exoplanet atmospheres. Absorption features in the transmission spectra of gas giant exoplanet atmospheres caused by the presence of these fingerprint ions may be observable with future observations with JWST (Gardner et al., 2006) and ARIEL (Tinetti et al., 2021). These observations could help constrain the cosmic ray fluxes reaching exoplanet atmospheres and give some constraints for simulations. Additionally, these observations could also help us to further piece together the habitability "puzzle".

1.5 This thesis

This thesis is about modelling the Galactic cosmic ray propagation through the winds of M dwarfs with an emphasis on modelling cosmic ray fluxes at the planet's orbit and the habitable zone. An outline of this thesis is presented next.

Chapter 2: Trends in stellar wind properties of M dwarfs

This chapter focuses on a parametric study of the winds of M dwarfs aiming to understand the general trends in the wind properties, such as the mass-loss rates, velocities, and temperatures. A 1D MHD Alfvén-wave driven stellar wind model was used to describe the stellar wind outflow. The input parameters are explored by varying the magnetic field strength and the wind density at the wind base, in this case at the chromosphere.

It is demonstrated that the temperature of our winds, driven by the presence of Alfvén waves, quickly reach an isothermal stage with mass-loss rates proportional to the wind base density, $\dot{M} \propto \rho_0^2$. Additionally, a comparison between our models and an isothermal wind model (Parker wind) is presented. It is shown that models with denser winds have terminal velocities and mass-loss rates values consistent with a Parker wind.

More rarefied winds, on the other hand, have their terminal velocities and mass-loss rate underestimated by a Parker wind. This implies that denser winds can be well described by simplified isothermal wind models.

Finally, using our wind models, the X-ray luminosity of the M dwarf GJ 436 was calculated by assuming that the luminosity is proportional to the radiative losses in the chromosphere. By comparing with observed X-ray luminosity, the mass-loss rate of GJ 436 was constrained to be $\dot{M} < 7.6 \times 10^{-15}\, M_{\odot}\ \mathrm{yr}^{-1}$. This value is compared with other models for the same star using different approaches.

This chapter was published in Monthly Notices as Mesquita & Vidotto (2020), 494, 1297–1307.

Chapter 3: The terrestrial Galactic cosmic ray flux in the habitable zone of GJ 436

This chapter explores the propagation of Galactic cosmic rays in the planetary system GJ 436. The flux of cosmic rays reaching different distances in GJ 436's astrosphere was quantified by using a 1D cosmic ray transport model. Because the stellar wind properties of GJ 436 are not well constrained, two stellar wind models from Chapter 2 were used, one with a mass-loss rate consistent with X-ray luminosity observations and another one with a higher mass-loss rate (by 2 orders of magnitude). However, the two stellar wind regimes have similar magnetic field and velocity profiles.

Although the astrosphere size calculated for each regime was different, one ten times larger than the other, the Galactic cosmic ray fluxes at the habitable zone and at GJ 436 b were found to be similar for both wind regimes. In addition, the flux at the habitable zone was found to be comparable with the intensities observed on Earth. However, because GJ 436 b has a close-in orbit the cosmic ray flux reaching the exoplanet was calculated to be ~ 10000 times smaller than observed values at Earth for cosmic rays with energy $\lesssim 3 \times 10^{-2}\,\mathrm{GeV}$.

This chapter was published in Monthly Notices as Mesquita et al. (2021), 505, 1817–1826.

Chapter 4: Galactic cosmic ray fluxes in M dwarf with known exoplanets

This chapter expands the study of Galactic cosmic ray propagation in five M dwarf astrospheres (GJ 15A, GJ 273, GJ 338B, GJ 411, and GJ 887). These stars were chosen because they have at least one detected exoplanet and their wind mass-loss rates are

constrained by Lyman-α observations. To determine a stellar wind with properties constrained by observations a 1D MHD Alfvén-wave-driven stellar wind model was used (previously used in Chapter 2). For the Galactic cosmic ray propagation, a 1D cosmic ray transport model was used (previously used in Chapter 3).

The habitable zone of GJ 411 and GJ 887 was found to receive comparable Galactic cosmic ray fluxes with Earth's value, while in GJ 15A, GJ 273, and GJ 338B the fluxes are lower. The Galactic cosmic ray fluxes received by almost all the planets in the sample are significantly lower than Earth's values as the planets have a close-in orbit. The exceptions are GJ 15A c, which has a slightly higher flux than Earth, and GJ 411 c, which receives Galactic cosmic ray fluxes similar to the LIS.

Finally, the radiation dose received at the surface was calculated for the only habitable-zone planet in the sample, GJ 273 b. By assuming an Earth-like atmosphere and no magnetic field, it was found that GJ 273 b receives a radiation dose equivalent to 40% of the annual dose on Earth's surface. This radiation dose is quite significant since GJ 273 b receives only ~ 2.3 times less GeV cosmic rays than Earth.

This chapter was published in Monthly Notices as Mesquita et al. (2022a), 509, 2091–2101.

Chapter 5: The effect of particle drift on Galactic cosmic ray propagation in M dwarf systems

In this chapter, the effect of particle drift is studied. Particle drifts are caused by gradients and curvatures in the stellar magnetic field that was incorporated in the Galactic cosmic ray propagation model. The study is focused on two M dwarfs: Prox Cen, the closest star in the solar neighbourhood, and AU Mic, a very young and active star. Both stars have known exoplanets, and in particular, Prox Cen b orbits in the habitable zone.

Particle drift was shown to affect the cosmic ray spectrum in M dwarf systems. In the case of Prox Cen and AU Mic, the inclusion of particle drift increased the intensity of Galactic cosmic rays in the astrosphere when compared with models without particle drift. This effect is more relevant for Prox Cen. Since the stellar wind properties of AU Mic are not well constrained, two wind environments were used (a high and a low stellar wind mass-loss rate). Both wind scenarios show a strong suppression of cosmic rays but they do not show similar modulation for the same distance. Galactic cosmic ray fluxes reaching Prox Cen b, AU Mic b and AU Mic c are strongly suppressed and, compared with Earth their fluxes are much smaller.

This chapter was published in Monthly Notices as Mesquita et al. (2022b), 515, 1218–1227.

1.6 Outlook

In this work, we have mainly used 1D stellar wind simulations and 1D cosmic ray transport models. 3D cosmic ray models are commonly used to describe cosmic ray transport in the heliosphere and to quantify the intensities at Earth (e.g., Potgieter, 2013). These models can help to understand the observations of Galactic cosmic rays at Earth and their effects. For this reason, a natural future step is to implement a 2D/3D model to better describe the 3D nature of the cosmic ray transport within other astrospheres. Since particle drifts seem to affect cosmic ray transport, the 3D cosmic ray models will further allow the inclusion of the three components of particle drift. 3D MHD simulations of stellar winds would also better characterise the system.

Stellar cosmic ray effects have been neglected in this work, however, it is expected that stellar cosmic ray fluxes dominate over Galactic cosmic rays up to a certain energy. This may be especially relevant for young and active stars which can accelerate stellar cosmic rays during flares and coronal mass ejections (Rodgers-Lee et al., 2021a). For this reason, the contribution of stellar cosmic rays should also be quantified for the M dwarfs studied here. In addition, Barth et al. (2021) showed that apart from fingerprint ions, stellar cosmic rays can also strongly enhance the abundance of organic molecules, such as formaldehyde (CH_2O) and ethylene (C_2H_2) which are both precursors to the production of glycine ($C_2H_5NO_2$). Glycine is one of the amino acids associated with the origin of life, originally produced in the Miller-Urey experiment (Miller, 1953). In particular, ethylene was enhanced to values possibly observable by spectroscopic atmosphere observations with JWST. Additionally, to interpret spectroscopic observations information from both cosmic ray fluxes (Galactic and stellar) will be needed.

Finally, Trappist-1 is a fascinating system with four habitable-zone planets in a total of seven planets. With so many possible habitable planets in a single system, it would be interesting to estimate the fluxes of Galactic and stellar cosmic rays reaching those exoplanets.